Scilight

Medical Acoustics and Imaging
https://www.sciltp.com/journals/mai



Article

A Compact 767 nm Excitation Source for Photoacoustic Microscopy

Lukasz A. Bugyi [1], Antti Penttinen [2], Antti Härkönen [2], Antti Rantaniemi [2], Jesse Koskinen [2], Stefan Schrittwieser [3], Qingliang Zhao [4], Stefanie Kirchberger [5], Andrea Wenninger-Weinzierl [5], Caterina Sturtzel [5,6], Richard Haindl [1], Wolfgang Drexler [1] and Mengyang Liu [1,*]

[1] Center for Medical Physics and Biomedical Engineering, Medical University of Vienna, Währinger Gürtel 18-20, AKH 4L, 1090 Vienna, Austria
[2] Picophotonics Ltd., Kauhakorvenkatu 53B, 33710 Tampere, Finland
[3] AIT Austrian Institute of Technology, Giefinggasse 4, 1210 Vienna, Austria
[4] School of Public Health, Xiamen University, Xiang'annanlu 4221, Xiping Building, Xiamen 361102, China
[5] Zebrafish Core Unit, St. Anna Kinderkrebsforschung GmbH, Zimmermannplatz 10, 1090 Vienna, Austria
[6] Zebrafish Platform Austria for Preclinical Drug Screening (ZANDR), Zimmermannplatz 10, 1090 Vienna, Austria
* Correspondence: mengyang.liu@meduniwien.ac.at

How To Cite: Bugyi, L.A.; Penttinen, A.; Härkönen, A.; et al. A Compact 767 nm Excitation Source for Photoacoustic Microscopy. *Medical Acoustics and Imaging* **2026**, *1*(1), 1.

Received: 18 September 2026
Revised: 13 November 2026
Accepted: 20 November 2026
Published: 24 November 2026

Abstract: Prussian blue nanoparticles (PBNP) have attracted extensive interest from biomedical researchers due to their favorable biocompatibility. However, the use of PBNP in photoacoustic microscopy (PAM) is limited due to the lack of commercially available excitation sources emitting in the peak absorption wavelength range of PBNP. In this work, we introduce a novel 767 nm excitation source with low cost and compact size. Using the seed wavelength of 1535 nm, the Q-switched microchip laser converts the seed wavelength to 767 nm with high efficiency. Operating at a pulse repetition rate of 1 kHz, the 767 nm output can reach an average power of 14 mW and a pulse duration of 3.8 ns. Its pulse-to-pulse energy variation is measured to be 1.9%. After laser characterization, *in vivo* PAM imaging using this source is performed on zebrafish larvae with PBNP injection, demonstrating this laser source's applicability in biomedical research.

Keywords: photoacoustic microscopy; laser; Prussian blue; zebrafish

1. Introduction

Unlike photoacoustic tomography, which often uses optical parametric oscillator (OPO) as the excitation source, photoacoustic microscopy (PAM) mostly relies on single wavelength excitation sources. Among all the available excitation wavelengths for PAM, 532 nm is still the dominant one due to the mature technology of Q-switched Nd:YAG lasers. However, the cost of such solid-state lasers is high, and a single wavelength prevents the use of spectroscopic PAM, whereas spectroscopic PAM presents a major advantage of this imaging modality [1]. To reduce the cost of the excitation source for PAM, many solutions have been offered, among which light-emitting diode (LED) and laser diode (LD) are the most popular. Although LEDs and LDs are much more affordable and can offer a plethora of wavelengths, the output energy from these sources is one to two orders of magnitude lower than that of solid-state lasers, hence severely limiting the achievable penetration depth [2]. Furthermore, the pulse duration of LED and LD is usually in the range of 30 ns to 100 ns, which means that the axial resolution of the PAM system based on these excitation sources is also limited [3]. Therefore, additional efforts, such as the use of a direct model inversion algorithm [4] or the dictionary learning technique [5] are needed to improve the axial resolution of PAM systems that use LED or LD as the excitation sources. Another alternative for PAM excitation is fiber lasers, whose gain media are optical fibers doped with rare-earth elements [6] or pure silica consisting of



Copyright: © 2026 by the authors. This is an open access article under the terms and conditions of the Creative Commons Attribution (CC BY) license (https://creativecommons.org/licenses/by/4.0/).
Publisher's Note: Scilight stays neutral with regard to jurisdictional claims in published maps and institutional affiliations.

a two-dimensional periodic air hole array to compose a photonic crystal fiber (PCF) [7]. Utilizing fiber nonlinearities, a fiber laser can be configured as a supercontinuum source emitting a broad spectrum [8], a stimulated Raman scattering (SRS) laser with several individual wavelengths emitted at the same time [9], or a Q-switched fiber laser with a single output wavelength [10]. Recently, an all-fiber SRS laser with three output wavelengths was demonstrated to provide functional PAM images successfully [11]. Despite all the advantages of fiber lasers, it is still technically challenging to provide excitation wavelengths in the near infrared (NIR) range with narrow linewidth and sufficient pulse energy, which are needed for deep penetration and high-resolution PAM imaging.

Knowing that in the NIR window I (NIR-I), there is low water absorption and reduced absorption from the endogenous absorbers compared to that in the visible range [12], a proper PAM excitation source in this biological window would be beneficial. To fully exploit the NIR-I for PAM, however, additional contrast agents will be needed. Among all the contrast agents that have been demonstrated for PAM, Prussian blue nanoparticles (PBNP) have been proven as an excellent contrast agent for PAM both *in vivo* and *in vitro* thanks to its peak absorption in the NIR-I [13]. As the base compound of Prussian blue capsules have been approved by the U.S. Food and Drug Administration (FDA) for the treatment of patients with internal contamination of radioactive/non-radioactive cesium and/or thallium exposure [14], PBNP holds a big potential for clinical approval in human use for photoacoustic imaging. Although there are no human trials involving PBNP-containing injectable agent for photoacoustic imaging yet, there is a plethora of photoacoustic imaging studies using PBNP on mammals [15,16], including mammals with human tissue [17], which have laid a solid foundation for using PBNP as a contrast agent in clinical photoacoustic imaging in the future [18].

Thus far, the use of PBNP in photoacoustics mostly relies on OPO or SRS sources emitting in the visible range [19–21]. For PAM applications using PBNP, a suitable excitation source emitting in the NIR-I range is still unavailable commercially. In this work, we introduce a newly-launched, commercially available compact pulsed laser emitting at 767 nm with a narrow linewidth, low-complexity monolithic cavity, and high repetition rate. The 767 nm output is achieved by second harmonic generation (SHG) of the 1535 nm seed light in a Q-switched microchip laser. Efficient SHG is enabled using a periodically poled lithium niobate (PPLN) crystal. After laser characterization, its applicability in PBNP visualization is demonstrated by *in vivo* imaging of zebrafish with PBNP solution injection.

2. Materials and Methods

2.1. Architecture of the 767 nm Laser

The schematic of the 767 nm laser is illustrated in Figure 1a. The core of the laser consists of a passively Q-switched 1535 nm laser kept at 19.5°C which is used as the seed source, whose 35 mW output goes through a half-wave plate and a condenser with a focal length of 12 mm. The SHG takes place in the 25 mm long PPLN, followed by a shortpass filter (FESH0850, Thorlabs, Newton, NJ, USA) and a collimator. The PPLN crystal's temperature is precisely controlled by a Peltier module. Two photos of the laser are given in Figure 1b,c, showing the dimension of the laser head as well as its power supply unit (PSU).

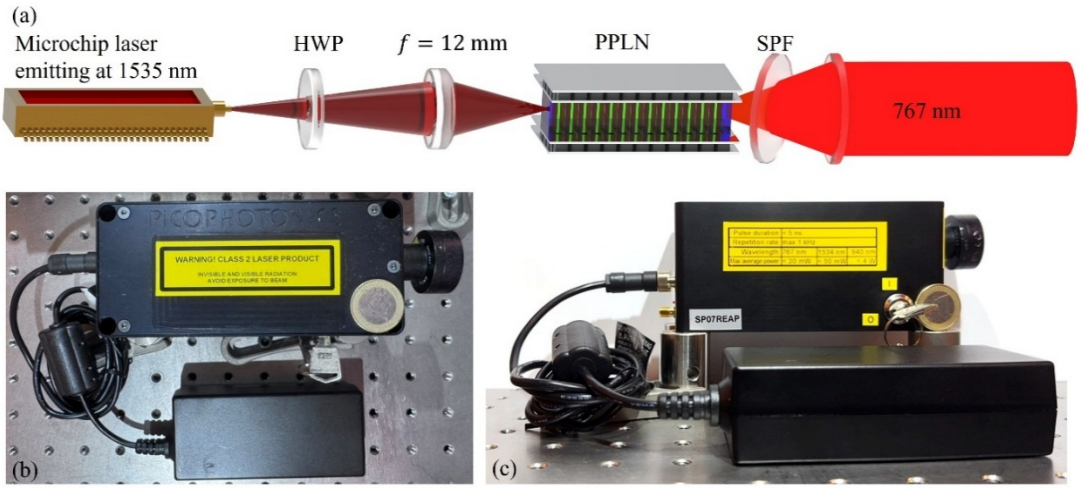

Figure 1. Architecture of the 767 nm laser. (**a**) The core components of the laser from the seed light to the collimator. (**b**) Top view of the laser and its PSU. (**c**) Side view of the laser head. HWP: half-wave plate; SPF: shortpass filter.

2.2. The PAM System

To verify the usability of the 767 nm laser for PAM application, the laser is connected to a previously reported PAM system [22]. A 3D schematic of the PAM system is given in Figure 2a, whereas a bird's eye view of how the laser is incorporated into the system is given in Figure 2b. In brief, the 767 nm laser output is coupled into a single mode fiber (P3-630Y-FC-2, Thorlabs) by two steering mirrors. Between these two mirrors, a 100 µm glass slide (CG00C2, Thorlabs) is used to reflect 4% of the laser energy to a homemade pulse detector to trigger data acquisition. The detector uses a photodiode (S12109-32, Hamamatsu, Hamamatsu City, Japan) to detect the pulse and the onboard circuitry generates a TTL signal for each detected pulse as an output trigger signal. In order to limit the pulse energy to a safe level for *in vivo* zebrafish imaging, the laser beam is attenuated using a variable neutral density filter (NDC-50C-4M, Thorlabs). To maximize the coupling efficiency between the free space light and the single mode fiber, a fiber launch (MAX313D/M, Thorlabs) is used, resulting in 29.8% coupling efficiency. In the scanning probe, the excitation light is firstly collimated by a reflective collimator (RC12FC-P01, Thorlabs) before being focused via a microscope objective (MY10X-803, Mitutoyo, Kawasaki, Japan). The transmission coefficient of this objective at 767 nm is experimentally measured to be 73.1%. The focusing beam propagates through a homemade ring transducer mounted on a kinematic mount. The confocal design of the ring transducer and the microscope objective shown in Figure 2c is used to maximize the sensitivity of the PAM system. A unique feature of the PAM system is that it follows a Lissajous scanning trajectory and is inherently correcting the laser jitter-induced distortion in the lateral directions. This feature is enabled by precise location tracking implemented via the encoder of the two scanning stages (DMQ12L-AE55T10A & LSM025A-E03T4A, Zaber Technologies, Vancouver, BC, Canada) and an FPGA (PXIe-5775, National Instruments, Austin, TX, USA). The FPGA labels each A-line record with sub-µm accuracy recorded at the time of optical pulse detection, thereby preventing jitter from impacting the reconstruction geometry. The tracking system stays active during fiber changing, providing the same reference positions across multiple acquisitions, and enabling co-registration of images acquired at different wavelengths. In this work, the oscillation frequencies in the fast and slow axes for the Lissajous trajectory are set to 11.09 Hz and 0.569 Hz, respectively. To characterize the PAM system performance when the 767 nm laser is implemented, a resolution target (R1DS1P1, Thorlabs) is used as the sample. Water is used as the couplant between the ring transducer and the resolution target. Other system performance specifications, such as imaging speed, field of view, and image reconstruction protocol are the same as described in our previous work [22].

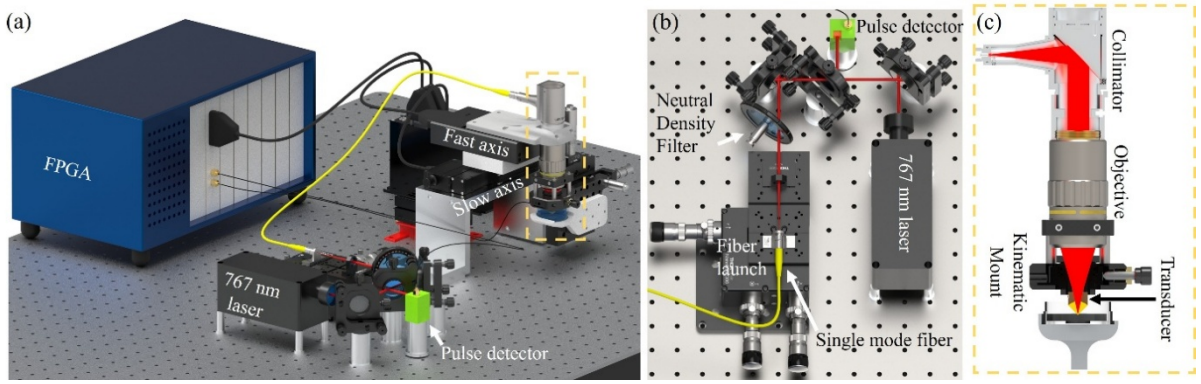

Figure 2. PAM system incorporating the 767 nm laser. (**a**) 3D schematic of the PAM system. (**b**) Bird's eye view of how the 767 nm laser output is coupled into the single mode fiber and detected by the pulse detector. (**c**) Partial cutaway view of the scanning probe marked by the dashed line in (**a**).

2.3. PBNP Characterization

The size of PBNP used in this work (XFJ103, XFNANO Materials Tech. Co., Nanjing, China) is measured by a scanning electron microscope (Supra 40, Carl Zeiss, Oberkochen, Germany) at 5 kV acceleration voltage using an in-lens detector. More specifically, an imaging sample of PBNP in aqueous solution is prepared by drop-casting a dispersion onto a Si wafer substrate (WSI04-0811003, Active Business Company, Marquartstein, Germany) with a native oxide surface and letting it dry at room temperature. The acquired images are then processed and analyzed using a homemade MATLAB script (r2025b, MathWorks, Natick, MA, USA) to evaluate the size distribution of PBNP. Optical absorption of the PBNP dispersion is measured by a Fourier transform infrared spectrometer (Vertex 70, Bruker Corporation, Billerica, MA, USA) equipped with an additional visible light source (64642 HLX, OSRAM Light, Munich, Germany) and a Si photodetector. Before measurement, PBNP dispersion is injected into a PMMA cuvette (67.742, Sarstedt AG & Co. KG, Nümbrecht, Germany) with 1 cm

optical pathlength. The incident beam propagates perpendicularly to the cuvette's surface, and a reference experiment is done by letting the incident beam propagate through the same type of cuvette filled with water. The measured PBNP absorption spectrum is then compared with a published soluble PBNP absorption spectrum [23].

2.4. Zebrafish Preparation

To verify the applicability of the 767 nm source for PBNP imaging in an *in vivo* environment, zebrafish larvae 5 days post fertilization (dpf) are used as the animal model. These transparent casper zebrafish (mpva17$^{a9/a9}$, mitfa$^{w2/w2}$), which lack melanocytes and iridophores are bred at St. Anna Kinderkrebsforschung GmbH in Vienna, Austria under licenses GZ:565304-2014-6 and GZ:534619-2014-4. To prepare the PBNP solution for micro-injections, PBNPs are first ultrasonicated for 30 s to disperse agglomerates. Then, PBNP solution is prepared with a PBNP concentration of 11.63 mM, which is within the published safety limit [24]. Zebrafish larvae at the age of 5 dpf are anesthetized with 320 mg/L tricaine solution for 3 min and then micro-injected with 2 nL of the prepared PBNP solution via a glass needle into the otic vesicle, which is a hollow epithelium cavity formed when ear placodal ectoderm cavitates. This location is chosen because it has been widely used in studies involving injecting zebrafish [25,26]. Afterwards, these larvae are mounted in glass-bottomed petri dishes (D35-14-1-N, Cellvis, Mountain View, CA, USA) with 1.5% agarose (A2576-5G, Sigma-Aldrich, St. Louis, MO, USA) at 28 °C, which are inserted into the imaging system.

2.5. PAM Imaging

For PAM imaging, tricaine solution is used as the acoustic couplant between the agarose and the ring transducer. In addition to the 767 nm source introduced in this work, we also employ a 532 nm source (SPOT-10-200-532, ElforLight, Daventry, UK) to perform the same imaging so that we may compare the results. For the 767 nm source, the repetition rate is 1 kHz and the pulse energy measured at the sample is 35 nJ. For the 532 nm source, the repetition rate is 10 kHz and the pulse energy measured at the sample is 60 nJ. To switch between the two excitation wavelengths, the single mode fiber connected to the collimator in the scanning probe also must be changed to maintain an acceptable transmission loss and dispersion. To image the zebrafish, a field of view of 1 mm × 0.8 mm is chosen. Due to the repetition rate difference, imaging at 532 nm takes 6.82 min, whereas imaging at 767 nm takes 34 min. The acquired images are first denoised using a median filter, and are then projected en face using standard deviation projection. To fuse the images acquired at 532 nm and 767 nm, two color channels are used with green allocated to 532 nm images and red allocated to 767 nm images. All image processing is done using routines provided by FIJI [27].

As of now, there is no commonly accepted laser safety standards available for zebrafish imaging. To be on the safe side, we calculated the average fluence value using parameters reported in other PAM imaging studies using zebrafish [28–33], which is 20.41 nJ/μm^2. In our experiment, by using a variable neutral density filter, we make sure that the optical fluence on the sample is below this average value, namely 17.82 nJ/μm^2 at 532 nm and 10.40 nJ/μm^2 at 767 nm.

3. Results

3.1. Laser Characterization

Operating at 1 kHz pulse repetition rate with the seed laser temperature set to 19.5 °C, the laser output reaches a maximum average power of 14 mW when the PPLN temperature is set to 47.7 °C, achieving 40% conversion efficiency. However, since the laser system responds to variation of temperature in the PPLN crystal with less power output change when the phase-matching temperature is offset to 46.5 °C, the following characterization is performed when the output average power is measured to be 6.5 mW, which gives the best stability for the output pulse energy. At this operation configuration which optimizes laser energy stability, the relevant conversion efficiency is 18.6%. The relative pulse energy variation is measured by using an energy meter (EnergyMax-USB J-10SI-HE, Coherent, Saxonburg, PA, USA) to record 1 million pulses continuously. The result is given in Figure 3a, showing a pulse-to-pulse energy variation of 1.9% by calculating the standard deviation of the pulse energies. To measure the pulse duration, the output of the laser is directed to a photodetector (DET025A/M, Thorlabs) after attenuation. The photodetector signal is then read by an oscilloscope (DSOX3104T, Keysight, Santa Rosa, CA, USA), whose representative reading is given in Figure 3b. Using the full width at half maximum (FWHM) as the result, the pulse duration is measured to be 3.8 ns. To measure the linewidth of the output, an optical spectrum analyzer (AQ6470E, Yokogawa Electric Corporation, Tokyo, Japan) is used. Centered at 767.47 nm, the linewidth is measured to be 0.04 nm, as indicated in Figure 3c. To measure the interval variations between consecutive

pulses, the output from the photodetector is read by another oscilloscope (MSO4054, RIGOL, Suzhou, China) which is controlled by a homemade MATLAB script (r2023b, MathWorks). The oscilloscope acquires 2000 pulses per record, and a total of 4000 records are acquired. The pulse-to-pulse time interval is plotted in Figure 3d. As shown in the figure, the interval can be as short as 990 µs and as long as 1035 µs, reflecting a relatively high level of jitter. Finally, the beam profile of the output is measured by a beam profiler (WinCam-D, DataRay Inc., Monterey, CA, USA), whose result is given in Figure 3e,f. Fitting Figure 3f to a Gaussian profile yields the results presented in Figure 3g with $R^2 = 0.979$.

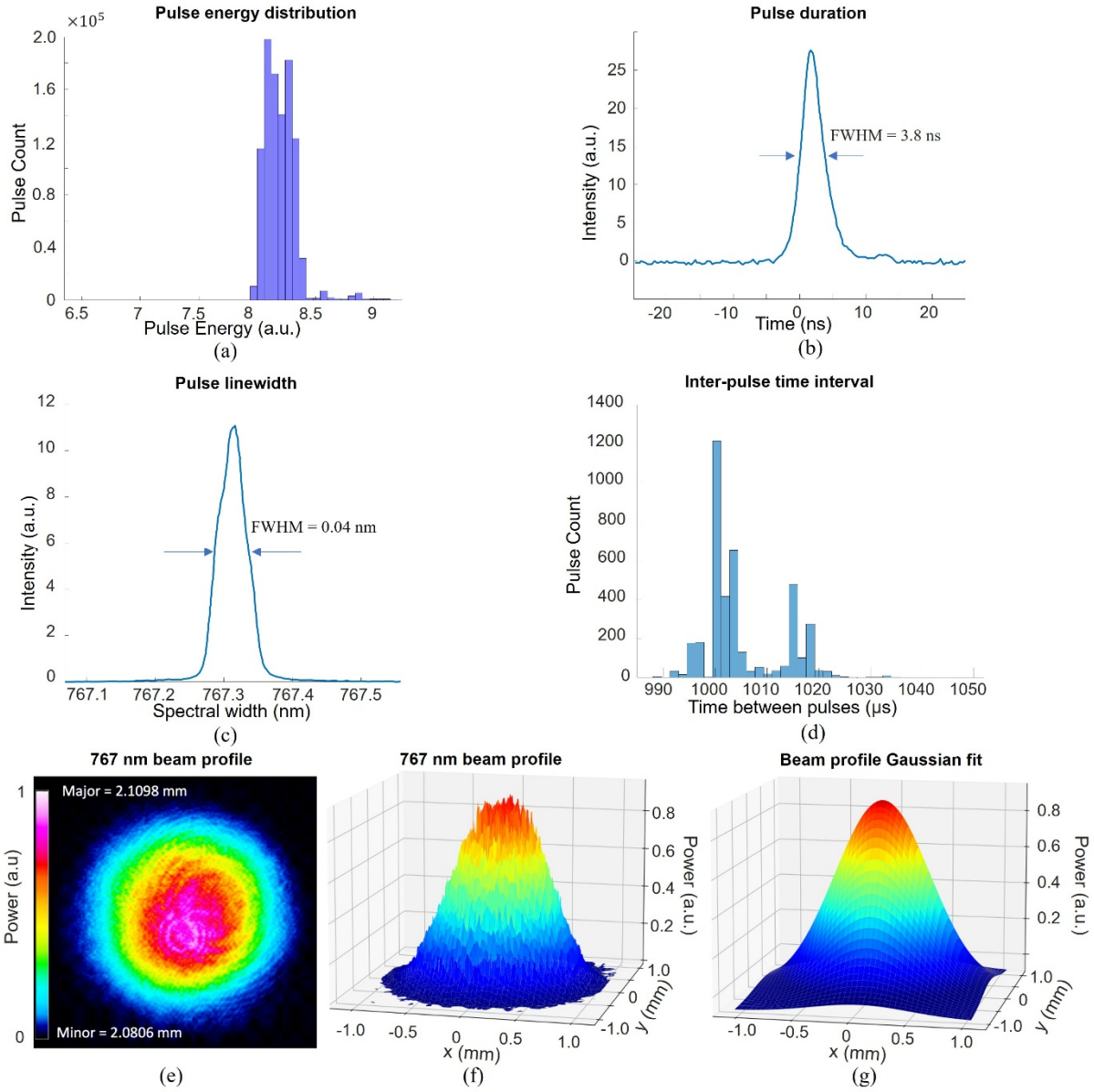

Figure 3. Characterization of the 767 nm laser output. (**a**) Pulse energy distribution of a total of 1 million consecutive pulses. (**b**) The pulse duration measurement of the 767 nm output. (**c**) The linewidth measurement. (**d**) The pulse-to-pulse interval distribution measurement. (**e**) The beam profile. (**f**) 3D view of the beam profile. (**g**) Gaussian fit of the beam profile.

3.2. PAM System Performance

The edge spread function (ESF) and the corresponding line spread function (LSF) by using the 767 nm source to image a sharp edge of the resolution target is shown in Figure 4a and 4b, respectively. To calculate the LSF, the raw data of the ESF is firstly fitted to a sigmoid function. The lateral resolution is then determined to be 2.07 µm for the 767 nm illumination. Figure 4c shows the 50-times-averaged photoacoustic signal generated by the chrome coating of the resolution target. A signal to noise ratio (SNR) of 43.02 dB is achieved, which is defined as the ratio of the peak-to-peak signal to the standard deviation of the noise floor. As a comparison, the single shot A-line

SNR is calculated to be 26.03 dB. The envelope of the photoacoustic signal is plotted in Figure 4d, which is then fitted to a Gaussian curve. By calculating the FWHM of the fitted curve, the axial resolution using 767 nm illumination is 41.16 µm. As a reference, the lateral resolution and the axial resolution when 532 nm is used as the excitation wavelength is reported to be 1.8 µm and 41.22 µm, respectively [22]. Despite the microscope objective being non-optimal for 767 nm, the spatial resolution of the PAM system stays very much the same for both 767 nm and 532 nm illuminations.

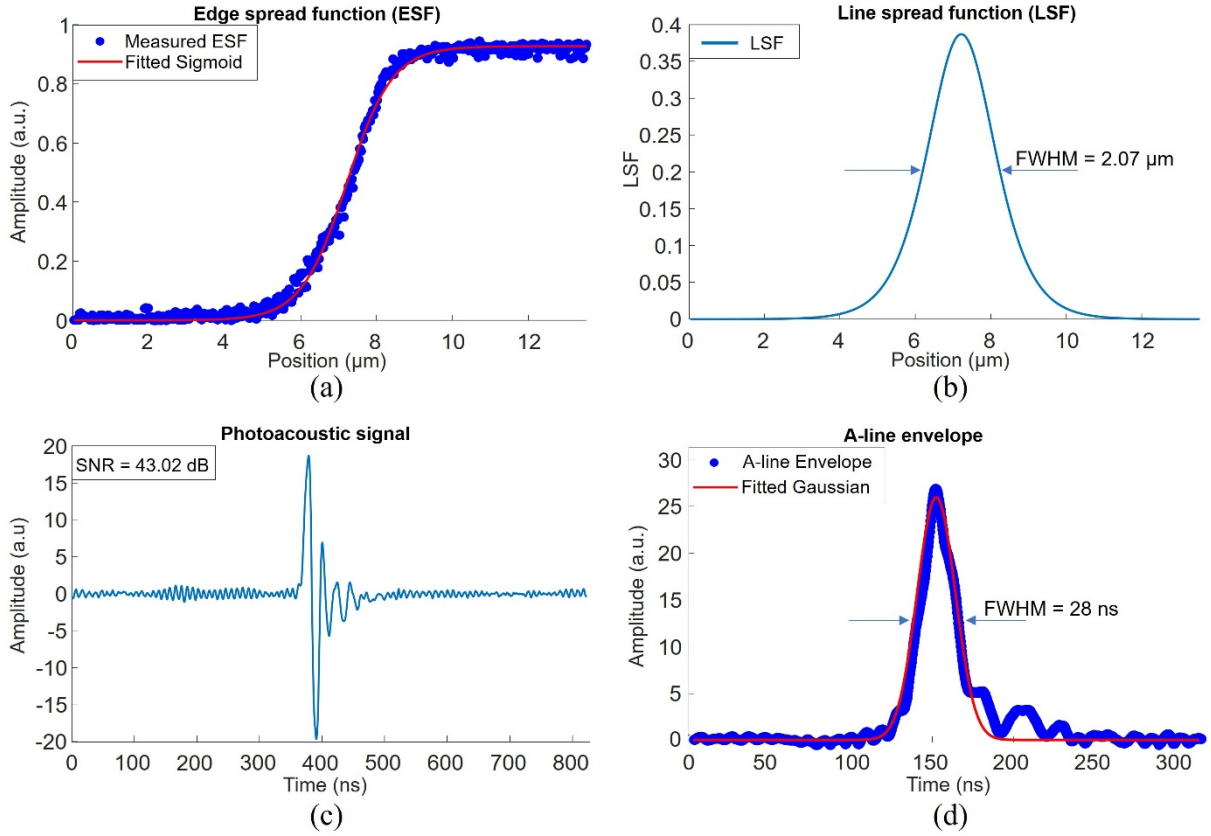

Figure 4. Spatial resolution and sensitivity measurements of the PAM system with 767 nm illumination. (**a**) Edge spread function by measuring a sharp edge of the resolution target. (**b**) Line spread function calculated using the fitted curve in (**a**). (**c**) Acquired photoacoustic signal with 50 times averaging. (**d**) The envelope and its Gaussian fit for the signal shown in (**c**).

3.3. PBNP Measurement

Figure 5 shows the measurement results of the PBNP used in this study. The scanning electron microscope image of the nanoparticles is given in Figure 5a. In Figure 5b, the absorption spectrum of the PBNP solution is compared to spectra of PBNP solutions of various particle sizes. As can be seen in this figure, the spectrum of the PBNP used in this work is similar to that of 40 nm particles [23]. At 767 nm and 532 nm, the absorption is 87.3% and 17.9% of the peak absorption, respectively. PBNP's size distribution is shown in Figure 5c. When fitted to a Gaussian curve, the edge length of the cubes used in this study centers at 69.96 nm with $\sigma = 18.43$ nm, which gives a 68% distribution interval of [51.53 nm, 88.42 nm].

3.4. In Vivo Zebrafish Larva Imaging

Four zebrafish larvae at 5 dpf are injected with PBNP and imaged *in vivo* by PAM. Both 532 nm and 767 nm excitation wavelengths are used. Because of the high absorption coefficient of PBNP at 767 nm, the injection spot can be clearly visualized when 767 nm is used as the excitation wavelength, as is shown in Figure 6a. Since the pigmented retina has a broad absorption spectrum, both 532 nm and 767 nm illuminations can pick up the photoacoustic signals generated in the eye region of the fish. Comparing Figure 6b with Figure 6a, we can see that photoacoustic signal generated by hemoglobin is only visible at 532 nm. Figure 6c–f show the merged images acquired at both excitation wavelengths for the four fish used in this study, with the red channel indicating the result from 767 nm illumination and the green channel indicating the result from 532 nm illumination. By

evaluating these images, the distribution of PBNP can be clearly mapped by the 767 nm illumination with good differentiation from the blood vessel signals acquired at 532 nm excitation. When the images acquired at both excitation wavelengths are merged, the distribution of PBNP is then visualized with a detailed background of the blood vessels and major organs. After the imaging session, the larvae are removed from agarose and put into a petri dish with fish water for observation over the next few hours. No visible damage to or change of behavior of the zebrafish larvae is observed afterwards.

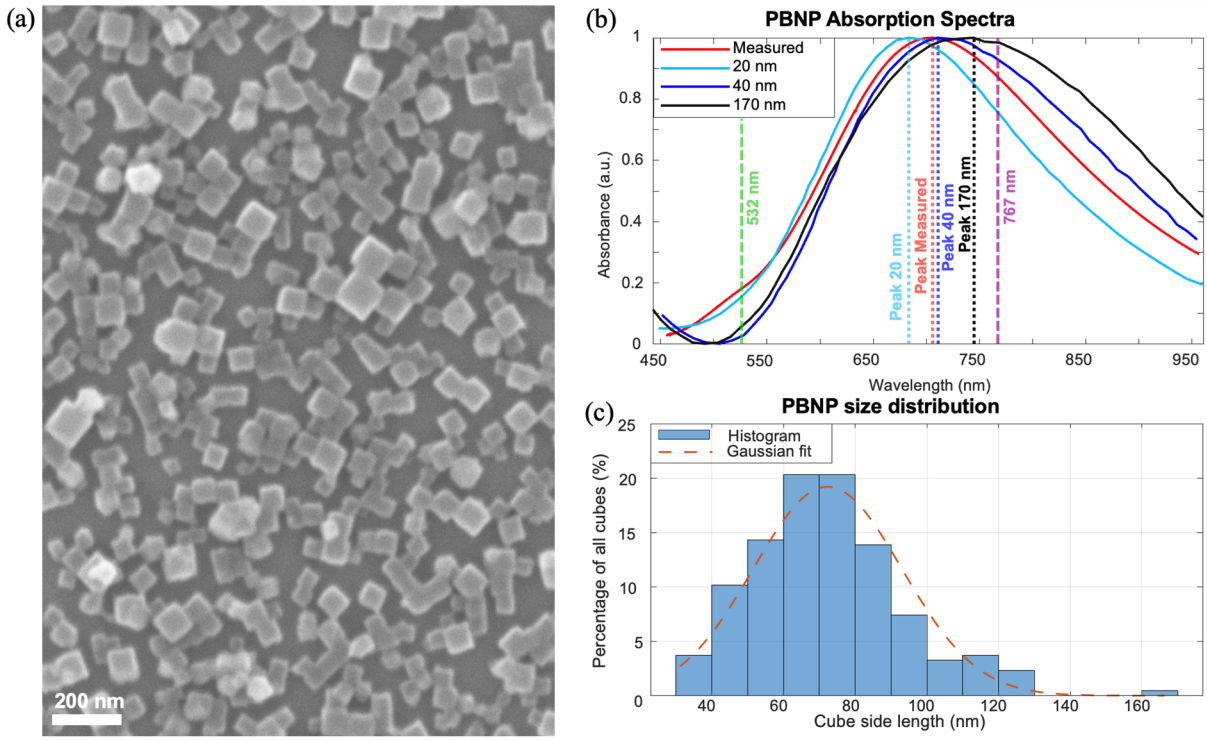

Figure 5. PBNP characterization. (**a**) A scanning electron microscope image of the PBNPs after drop-casting onto a Si substrate and drying. Scalebar: 200 nm; magnification: 150 K X; EHT: 5 kV; WD: 5.6 mm; Signal A = InLens. (**b**) Absorption spectra of the PBNP used in this study (red) and those reported in literature (blue). Adapted with permission from [23]. Copyright 2019, Elsevier Inc. The purple dotted vertical line indicates 767 nm. The green dotted vertical line indicates 532 nm. (**c**) Edge length distribution of the PBNP used in this study, which is calculated based on 216 cubes detected by an homemade image analysis script in MATLAB (2025b, MathWorks).

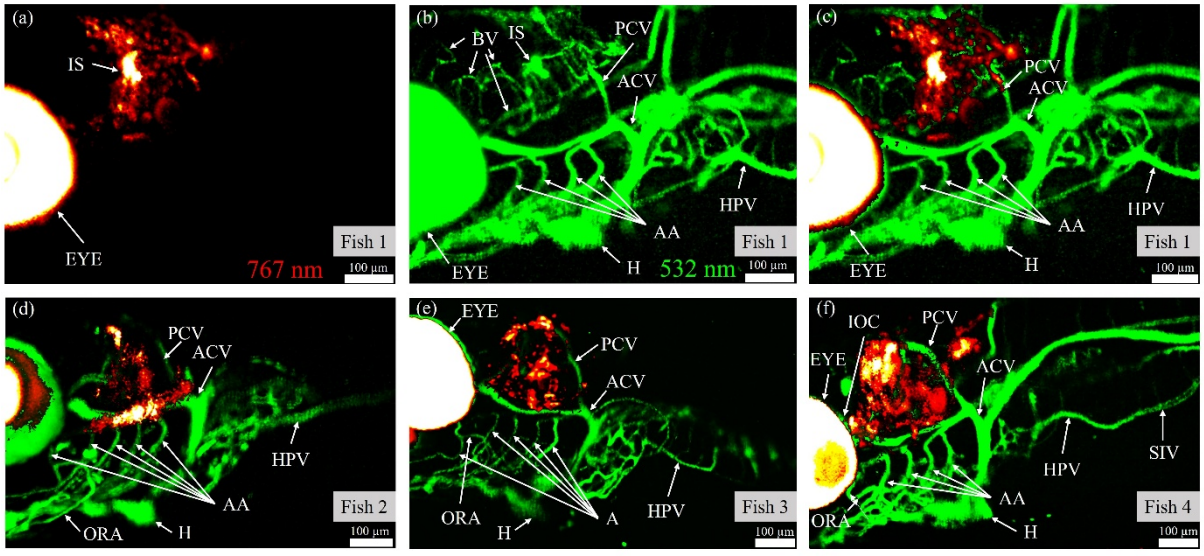

Figure 6. PAM imaging results of four 5 dpf zebrafish larvae. (**a**) The 767 nm PAM imaging result of fish 1. (**b**) The 532 nm PAM imaging result of fish 1. (**c**) Merged image of (**a**) and (**b**). (**d**) Merged PAM image of fish 2 with both 532 nm (green) and 767 nm (red) illuminations. (**e**) Merged PAM image of fish 3 with both 532 nm (green)

and 767 nm (red) illuminations. (**f**) Merged PAM image of fish 4 with both 532 nm (green) and 767 nm (red) illuminations. PCV: posterior cardinal vein; ACV: anterior cardinal vein; AA: aortic arches; HPV: hepatic port vein; ORA: opercular artery; H: heart; IOC: inner optic circle; SIV: subintestinal vein; BV: brain vessel; IS: injection spot.

4. Discussion

The 767 nm laser head has a dimension of 13.5 cm × 6 cm × 6.5 cm. Its PSU has a size of 11.5 cm × 5 cm × 3.5 cm. Compared with the commercial SRS source used in a similar PAM study using PBNP [21], whose laser head measures 24 cm × 12 cm × 5.5 cm with a PSU of 26 cm × 35 cm × 12 cm, the laser source introduced in this work is 17 times smaller in size. Compared with other diode-pumped solid-state (DPSS) PAM excitation sources that emit in the visible range, this 767 nm source is also much more compact. The smaller size and the relatively easy configuration make the 767 nm source advantageous for PAM applications that require a portable device with miniaturized footprint.

Currently, the 767 nm source can only reach a pulse repetition rate of 1 kHz, which is significantly lower than that of the DPSS sources used for PAM. However, since the seed microchip laser can be configured to operate at much higher repetition rates, the next generation of the 767 nm laser will be improved to increase the pulse repetition rate to 10 kHz. Another limitation of this first version 767 nm source is that it does not operate under external triggers, hence a pulse detector is needed to synchronize data acquisition. This issue can be tackled in the future by using laser jitter effect correction [34]. Although the jitter issue represented in Figure 3d is a downside, the 1.9% pulse energy variation over prolonged acquisitions eliminates the need for pulse energy normalization, which is generally requested for quantitative analysis of the PAM signal [35,36]. Notwithstanding, it is worth noting that this low variability of pulse energy is achieved by detuning the PPLN's operation temperature from the one that corresponds to the maximum PPLN conversion efficiency. This detuning is inherently needed due to the quasi-phase-matched SHG in the PPLN [37]. To increase the output power while maintaining low pulse-to-pulse energy variation, the next generation 767 nm source will need improved PPLN temperature control to enable sufficient stability at PPLN's peak conversion efficiency. As a comparison, the conversion efficiency reported in this work is comparable to that reported using a $KTiOPO_4$ crystal for SHG [38]. However, the peak conversion efficiency of PPLN is twice that of the $KTiOPO_4$ crystal. Another advantage of the 767 nm laser is its narrow linewidth of just 0.04 nm, which is two orders of magnitude narrower than that of the SRS source [39,40], and about three to four orders of magnitude narrower than that of LED and LD sources [41,42]. This extremely narrow linewidth can improve the accuracy of the spectral unmixing process in spectroscopic PAM studies by limiting spectral averaging [43,44]. In addition, the monolithic microchip design lowers the manufacturing cost and complexity by removing the optical alignment step. This is further supported by the passive Q-switching mechanism, which works without control electronics and optical switches. Finally, as seen in Table 1, this work demonstrates for the first time a PPLN-based 767 nm laser used for *in vivo* PAM imaging. Compared with other 767 nm sources that are used for PAM imaging, this new source has significant advantages in terms of repetition rate, pulse duration, and linewidth.

Table 1. Comparison of 767 nm excitation source specifications.

Specification	This Work	Pan et al. [45]	Boucon et al. [46]	Lee et al. [47]	Huang et al. [38]
Repetition rate	1 kHz	10 Hz	3.3 kHz	10 kHz	5 Hz
Pulse duration	3.8 ns	<15 ns	3 ns	7.6 ns	10 ns
Pulse energy	14 μJ	>17.85 mJ	0.5 μJ	162 μJ	2.7 mJ
Linewidth	0.04 nm	Not given	~4 nm	0.3 nm	2.9 nm
Technology	PPLN	Ti:sapphire	PPLN + PCF	NCPM LBO	$KTiOPO_4$
Contrast agent	PBNP	Gold nanoparticle	Not used	Not used	Indocyanine green
Biological sample imaged	Zebrafish	Rat	Not demonstrated	Not demonstrated	Human
Commercial availability	Yes	Yes	No	No	No
Dimension (cm × cm × cm)	13.5 × 6 × 6.5	>47 × 26 × 9	Not given	40 × 35.5 × 63.5	11 × 4 × 2.4

In this work, we choose PBNP as the contrast agent due to its strong absorption in the NIR range and its readily demonstrated usage in magnetic resonance imaging (MRI) [48,49]. PAM with 767 nm excitation

complements MRI by revealing the distribution of PBNP at a much finer spatial resolution, thereby allowing more precise information for PBNP-labeled regions in preclinical tumor models. The specific PBNP batch used in this study has a peak absorption wavelength corresponding to that of PBNP about 40 nm in size. As a comparison, the Gaussian fit to the edge-length distribution obtained from scanning electron microscopy of the dried sample is centered at approximately 70 nm in Figure 5c. This discrepancy might be caused by uncontrolled pH of the PBNP solution [50]. Another possible explanation is that the agglomerates in the dried sample may have been segmented as single objects, biasing the estimate toward larger sizes. Apart from PBNP, indocyanine green (ICG), whose peak absorption lies in NIR-I, is another possible contrast agent for the 767 nm PAM system. The use of ICG in PAM application is already successfully demonstrated [51]. Knowing that ICG is commonly used in fluorescence microscopy in both preclinical [52] and clinical settings [53], and that integrated photoacoustic and fluorescence microscopy is readily available [54,55], this 767 nm source has the potential to boost the applicability of PAM in more preclinical and surgical scenarios in the future. Except PBNP and ICG, a plethora of engineered contrast agents in the form of gold nanoparticles [56,57] and semiconductor polymer nanoparticles [58] can also benefit from the 767 nm excitation. Furthermore, since spectral domain optical coherence tomography (SD-OCT) usually uses light sources centered around 800 nm, integrating 767 nm PAM excitation source into readily demonstrated optical coherence PAM (OC-PAM) systems [22,30,32,59,60] would request minimal change of the system optics, and should provide better system performance than OC-PAM systems that uses 532 nm excitation sources.

In this work, image from 532 nm delineates the blood vessel distribution, whereas image from 767 nm visualizes PBNP distribution. This result predicts that, in tumor models, this dual wavelength approach could be used to examine the distribution of contrast agents with regard to the vascular network. Repeated imaging after PBNP administration can then help track changes associated with the nanoparticle deposition rates and washout rates [61]. Zebrafish is chosen for the feasibility study because it represents one of the most popular animal models used for biomedical research [62]. In the imaging results of 767 nm illumination, the distribution of PBNP covers an area larger than the otic vesicle, which is most likely due to the large injection needle tip and the leakage of PBNP into surrounding tissues. Because PBNP can be biofunctionalized as a molecular imaging agent [48], future research requires surface modification of PBNP before injection into zebrafish, so that the biofunctionalized PBNP can be used as an actual molecular contrast agent for PAM to study various pathophysiological processes in zebrafish.

5. Conclusions

A compact 767 nm pulsed laser source is characterized and then demonstrated in PAM imaging. The narrow linewidth, short pulse duration, low pulse-to-pulse energy variation, and quasi-Gaussian beam profile of the laser make it a useful source for PAM applications in the NIR-I range. This wavelength also means that PAM system using this excitation source can be easily integrated with fluorescence microscopy and SD-OCT. PBNP is used as the contrast agent in this work, which is successfully visualized in zebrafish imaging, warranting future studies using biofunctionalized PBNP in this animal model.

Author Contributions

L.A.B.: Experiment design, system design, system characterization, data acquisition, image reconstruction, methodology, writing—original draft; A.P.: Writing—review & editing, laser design, laser characterization, funding acquisition; A.H.: Writing—review & editing, laser design, laser characterization; A.R.: Laser characterization; J.K.: Laser characterization; S.S.: Nanoparticle characterization; Q.Z.: Writing—review & editing; S.K.: Writing—review & editing, fish preparation, figure annotation; A.W.-W.: Writing—review & editing, fish preparation, figure annotation; C.S.: Writing—review & editing, fish preparation, figure annotation; R.H.: Writing—review & editing, supervision; W.D.: Supervision, funding acquisition; M.L.: Writing—original draft, writing—review & editing, conceptualization, supervision, project management, funding acquisition. All authors have read and agreed to the published version of the manuscript.

Funding

This work is funded by the EU H2020-ICT project REAP with Grant Agreement ID 101016964, the H2020-FETOPEN project SWIMMOT with Grant Agreement ID 899612, and the Horizon Europe project ESOHISTO with Grant Agreement ID 101186952. It is also supported by the Medical University of Vienna Φocus projects COCTAIL and OASIS. The ZANDR platform (supported by the Austrian Research Promotion Agency (FFG) project 7940628 533 (Danio4Can)) of the Zebrafish Core Unit of St. Anna Children's Cancer Research Institute supported with zebrafish larvae and injection services presented in this publication.

Institutional Review Board Statement

Ethical review and approval were waived for this study, due to the larvae used were 5dpf or younger.

Informed Consent Statement

Not applicable.

Data Availability Statement

The research data can be made available upon request.

Conflicts of Interest

Antti Penttinen and Antti Härkönen are the CEO and CTO of Picophotonics Ltd., respectively. Antti Rantaniemi and Jesse Koskinen are employees of Picophotonics Ltd. Other co-authors declare no conflict of interest. Given the role as Associate Editor, Mengyang Liu had no involvement in the peer review of this paper and had no access to information regarding its peer-review process. Full responsibility for the editorial process of this paper was delegated to another editor of the journal.

Use of AI and AI-Assisted Technologies

No AI tools were utilized for this paper.

References

1. Park, E.; Kim, D.; Ha, M.; et al. A comprehensive review of high-performance photoacoustic microscopy systems. *Photoacoustics* **2025**, *44*, 100739. https://doi.org/10.1016/j.pacs.2025.100739.
2. Kuniyil Ajith Singh, M.; Xia, W. Portable and Affordable Light Source-Based Photoacoustic Tomography. *Sensors* **2020**, *20*, 6173. https://doi.org/10.3390/s20216173.
3. Wang, L.V. Tutorial on Photoacoustic Microscopy and Computed Tomography. *IEEE J. Sel. Top. Quantum Electron.* **2008**, *14*, 171–179. https://doi.org/10.1109/jstqe.2007.913398.
4. Navarro-Calvo, J.A.; Cebrecos, A.; Arándiga, A.; et al. Cost-effective laser diode scanning 3D photoacoustic microscopy of melanocytic dermal tumors *in situ*. *Ultrasonics* **2026**, *158*, 107831. https://doi.org/10.1016/j.ultras.2025.107831.
5. Farnia, P.; Najafzadeh, E.; Hariri, A.; et al. Dictionary learning technique enhances signal in LED-based photoacoustic imaging. *Biomed. Opt. Express* **2020**, *11*, 2533–2547. https://doi.org/10.1364/boe.387364.
6. Zervas, M.N.; Codemard, C.A. High Power Fiber Lasers: A Review. *IEEE J. Sel. Top. Quantum Electron.* **2014**, *20*, 219–241. https://doi.org/10.1109/jstqe.2014.2321279.
7. Wadsworth, W.J.; Ortigosa-Blanch, A.; Knight, J.C.; et al. Supercontinuum generation in photonic crystal fibers and optical fiber tapers: A novel light source. *J. Opt. Soc. Am. B* **2002**, *19*, 2148–2155. https://doi.org/10.1364/josab.19.002148.
8. Billeh, Y.N.; Liu, M.; Buma, T. Spectroscopic photoacoustic microscopy using a photonic crystal fiber supercontinuum source. *Opt. Express* **2010**, *18*, 18519–18524. https://doi.org/10.1364/oe.18.018519.
9. Koeplinger, D.; Liu, M.; Buma, T. Photoacoustic microscopy with a pulsed multi-color source based on stimulated Raman scattering. In Proceedings of the 2011 IEEE International Ultrasonics Symposium (IUS), Orlando, FL, USA, 18–21 October 2011; pp. 296–299. https://doi.org/10.1109/ultsym.2011.0071.
10. Jin, L.; Liang, Y. Fiber laser technologies for photoacoustic microscopy. *Vis. Comput. Ind. Biomed. Art* **2021**, *4*, 11. https://doi.org/10.1186/s42492-021-00076-y.
11. Yang, M.; Qu, Z.; Amjadian, M.; et al. All-fiber three-wavelength laser for functional photoacoustic microscopy. *Photoacoustics* **2025**, *42*, 100703. https://doi.org/10.1016/j.pacs.2025.100703.
12. Du, J.; Yang, S.; Qiao, Y.; et al. Recent progress in near-infrared photoacoustic imaging. *Biosens. Bioelectron.* **2021**, *191*, 113478. https://doi.org/10.1016/j.bios.2021.113478.
13. Liang, X.; Deng, Z.; Jing, L.; et al. Prussian blue nanoparticles operate as a contrast agent for enhanced photoacoustic imaging. *Chem. Commun.* **2013**, *49*, 11029–11031. https://doi.org/10.1039/c3cc42510j.
14. U.S. Food & Drug Administration. Media Inquiries: 301-827-6242, FDA Approves First New Drug Application for Treatment of Radiation Contamination Due to Cesium or Thallium. 2003. Available online: https://www.fda.gov/drugs/bioterrorism-and-drug-preparedness/fda-approves-first-new-drug-application-treatment-radiation-contamination-due-cesium-or-thallium (accessed on 30 June 2026).
15. Fu, G.; Liu, W.; Li, Y.; et al. Magnetic Prussian Blue Nanoparticles for Targeted Photothermal Therapy under Magnetic Resonance Imaging Guidance. *Bioconjug. Chem.* **2014**, *25*, 1655–1663. https://doi.org/10.1021/bc500279w.

16. Shou, P.; Yu, Z.; Wu, Y.; et al. Zn^{2+} Doped Ultrasmall Prussian Blue Nanotheranostic Agent for Breast Cancer Photothermal Therapy under MR Imaging Guidance. *Adv. Healthc. Mater.* **2020**, *9*, 1900948. https://doi.org/10.1002/adhm.201900948.
17. Kubelick, K.P.; Emelianov, S.Y. Prussian blue nanocubes as a multimodal contrast agent for image-guided stem cell therapy of the spinal cord. *Photoacoustics* **2020**, *18*, 100166. https://doi.org/10.1016/j.pacs.2020.100166.
18. Merino, V.F.; Saini, N.; Fernandes, R. Advancing prussian blue nanoparticle-mediated photothermal therapy through machine learning and multiomics integration. *Nanomedicine* **2026**, *21*, 823–838. https://doi.org/10.1080/17435889.2026.2628239.
19. Kim, T.; Lemaster, J.E.; Chen, F.; et al. Photoacoustic Imaging of Human Mesenchymal Stem Cells Labeled with Prussian Blue–Poly(L-lysine) Nanocomplexes. *ACS Nano* **2017**, *11*, 9022–9032. https://doi.org/10.1021/acsnano.7b03519.
20. Chen, L.; Tang, S.; Zhang, J.; et al. Prussian Blue Nanohybridized Multicellular Spheroids as Composite Engraftment for Antioxidant Bone Regeneration and Photoacoustic Tomography. *ACS Nano* **2024**, *18*, 24770–24783. https://doi.org/10.1021/acsnano.3c06835.
21. Bui, N.Q.; Cho, S.W.; Moorthy, M.S.; et al. *In vivo* photoacoustic monitoring using 700-nm region Raman source for targeting Prussian blue nanoparticles in mouse tumor model. *Sci. Rep.* **2018**, *8*, 2000. https://doi.org/10.1038/s41598-018-20139-0.
22. Bugyi, L.; Schmitner, N.; Kimmel, R.A.; et al. Lissajous-trajectory scanning optical coherence photoacoustic microscopy for zebrafish larva imaging. *J. Phys. Photonics* **2026**, *8*, 015042. https://doi.org/10.1088/2515-7647/ae392c.
23. Dumani, D.S.; Cook, J.R.; Kubelick, K.P.; et al. Photomagnetic Prussian blue nanocubes: Synthesis, characterization, and biomedical applications. *Nanomed. Nanotechnol. Biol. Med.* **2020**, *24*, 102138. https://doi.org/10.1016/j.nano.2019.102138.
24. Pearce, J. Studies of any toxicological effects of Prussian blue compounds in mammals—A review. *Food Chem. Toxicol.* **1994**, *32*, 577–582. https://doi.org/10.1016/0278-6915(94)90116-3.
25. Harvie, E.A.; Green, J.M.; Neely, M.N.; et al. Innate Immune Response to Streptococcus iniae Infection in Zebrafish Larvae. *Infect. Immun.* **2013**, *81*, 110–121. https://doi.org/10.1128/iai.00642-12.
26. Gillies, S.; Verdon, R.; Stone, V.; et al. Transgenic zebrafish larvae as a non-rodent alternative model to assess pro-inflammatory (neutrophil) responses to nanomaterials. *Nanotoxicology* **2022**, *16*, 333–354. https://doi.org/10.1080/17435390.2022.2088312.
27. Schindelin, J.; Arganda-Carreras, I.; Frise, E.; et al. Fiji: An open-source platform for biological-image analysis. *Nat. Methods* **2012**, *9*, 676–682. https://doi.org/10.1038/nmeth.2019.
28. Ye, S.; Yang, R.; Xiong, J.; et al. Label-free imaging of zebrafish larvae *in vivo* by photoacoustic microscopy. *Biomed. Opt. Express* **2012**, *3*, 360–365. https://doi.org/10.1364/boe.3.000360.
29. Moore, M.J.; El-Rass, S.; Xiao, Y.; et al. Simultaneous ultra-high frequency photoacoustic microscopy and photoacoustic radiometry of zebrafish larvae *in vivo*. *Photoacoustics* **2018**, *12*, 14–21. https://doi.org/10.1016/j.pacs.2018.08.004.
30. Haindl, R.; Deloria, A.J.; Sturtzel, C.; et al. Functional optical coherence tomography and photoacoustic microscopy imaging for zebrafish larvae. *Biomed. Opt. Express* **2020**, *11*, 2137–2151. https://doi.org/10.1364/boe.390410.
31. Yang, W.; Wang, W.; Jing, L.; et al. Label-free photoacoustic microscopy: A potential tool for the live imaging of blood disorders in zebrafish. *Biomed. Opt. Express* **2021**, *12*, 3643–3657. https://doi.org/10.1364/boe.425994.
32. Deng, S.; Haindl, R.; Zhang, E.; et al. An optical coherence photoacoustic microscopy system using a fiber optic sensor. *APL Photonics* **2021**, *6*, 096103. https://doi.org/10.1063/5.0059351.
33. Nguyen, V.T.; Taboada, C.; Delia, J.; et al. Dual-channel high-speed functional photoacoustic microscopy with ultra-wide field of view. *Light Sci. Appl.* **2026**, *15*, 91. https://doi.org/10.1038/s41377-025-02114-3.
34. Asadollahi, A.; Latifi, H.; Pramanik, M.; et al. Axial accuracy and signal enhancement in acoustic-resolution photoacoustic microscopy by laser jitter effect correction and pulse energy compensation. *Biomed. Opt. Express* **2021**, *12*, 1834–1845. https://doi.org/10.1364/boe.419564.
35. Wang, T.; Sun, N.; Cao, R.; et al. Multiparametric photoacoustic microscopy of the mouse brain with 300-kHz A-line rate.. *Neurophotonics* **2016**, *3*, 045006. https://doi.org/10.1117/1.nph.3.4.045006.
36. Li, X.; Kot, J.C.K.; Tsang, V.T.C.; et al. Ultraviolet photoacoustic microscopy with tissue clearing for high-contrast histological imaging. *Photoacoustics* **2022**, *25*, 100313. https://doi.org/10.1016/j.pacs.2021.100313.
37. Fejer, M.M.; Magel, G.A.; Jundt, D.H.; et al. Quasi-phase-matched second harmonic generation: Tuning and tolerances. *IEEE J. Quantum Electron.* **1992**, *28*, 2631–2654. https://doi.org/10.1109/3.161322.
38. Huang, Y.; Huang, L.; Zhong, R. Low-cost and compact second harmonic laser for photoacoustic imaging. *Biomed. Opt. Express* **2025**, *16*, 3499–3509. https://doi.org/10.1364/boe.574014.
39. Liang, Y.; Jin, L.; Guan, B.O.; et al. 2 MHz multi-wavelength pulsed laser for functional photoacoustic microscopy. *Opt. Lett.* **2017**, *42*, 1452–1455. https://doi.org/10.1364/ol.42.001452.
40. Hajireza, P.; Forbrich, A.; Zemp, R. *In-Vivo* functional optical-resolution photoacoustic microscopy with stimulated Raman scattering fiber-laser source. *Biomed. Opt. Express* **2014**, *5*, 539–546. https://doi.org/10.1364/boe.5.000539.
41. Li, X.; Tsang, V.T.C.; Kang, L.; et al. High-speed high-resolution laser diode-based photoacoustic microscopy for *in vivo* microvasculature imaging. *Vis. Comput. Ind. Biomed. Art* **2021**, *4*, 1. https://doi.org/10.1186/s42492-020-00067-5.

42. Singh, M.K.A.; Sato, N.; Ichihashi, F.; et al. The Evolution of LED-based Photoacoustic Imaging: From Labs to Clinics. In *Biomedical Photoacoustics: Technology and Applications*; Springer Nature: Cham, Switzerland, 2024; pp. 573–608. https://doi.org/10.1007/978-3-031-61411-8_22.
43. Cox, B.T.; Laufer, J.G.; Beard, P.C.; et al. Quantitative spectroscopic photoacoustic imaging: A review. *J. Biomed. Opt.* **2012**, *17*, 061202. https://doi.org/10.1117/1.jbo.17.6.061202.
44. Hirasawa, T.; Tachi, K.; Miyashita, M.; et al. Spectroscopic photoacoustic microscopic imaging during single spatial scan using broadband excitation light pulses with wavelength-dependent time delay. *Photoacoustics* **2022**, *26*, 100364. https://doi.org/10.1016/j.pacs.2022.100364.
45. Pan, D.; Pramanik, M.; Senpan, A.; et al. Near infrared photoacoustic detection of sentinel lymph nodes with gold nanobeacons. *Biomaterials* **2010**, *31*, 4088–4093. https://doi.org/10.1016/j.biomaterials.2010.01.136.
46. Boucon, A.; Sylvestre, T.; Huy, K.P.; et al. Supercontinuum generation by nanosecond dual-pumping near the two zero-dispersion wavelengths of a photonic crystal fiber. *Opt. Commun.* **2011**, *284*, 467–470. https://doi.org/10.1016/j.optcom.2010.09.035.
47. Lee, W.; Geng, J.; Qiang, Z.; et al. A Fiber-Based High-Power Single Frequency Pulsed Laser at 780 nm/776 nm for Rb Dating. *IEEE Photonics Technol. Lett.* **2019**, *31*, 1534–1537. https://doi.org/10.1109/lpt.2019.2937270.
48. Dumont, M.F.; Hoffman, H.A.; Yoon, P.R.; et al. Biofunctionalized Gadolinium-Containing Prussian Blue Nanoparticles as Multimodal Molecular Imaging Agents. *Bioconjug. Chem.* **2014**, *25*, 129–137. https://doi.org/10.1021/bc4004266.
49. Li, Z.; Zeng, Y.; Zhang, D.; et al. Glypican-3 antibody functionalized Prussian blue nanoparticles for targeted MR imaging and photothermal therapy of hepatocellular carcinoma. *J. Mater. Chem. B* **2014**, *2*, 3686–3696. https://doi.org/10.1039/c4tb00516c.
50. Colombi, C.; Dacarro, G.; Diaz Fernandez, Y.A.; et al. Human Serum Albumin Protein Corona in Prussian Blue Nanoparticles. *Nanomaterials* **2024**, *14*, 1336. https://doi.org/10.3390/nano14161336.
51. Zhong, J.; Yang, S. Contrast-enhanced photoacoustic imaging using indocyanine green-containing nanoparticles. *J. Innov. Opt. Health Sci.* **2014**, *07*, 1350029. https://doi.org/10.1142/s1793545813500296.
52. Fang, C.; Wang, K.; Zeng, C.; et al. Illuminating necrosis: From mechanistic exploration to preclinical application using fluorescence molecular imaging with indocyanine green. *Sci. Rep.* **2016**, *6*, 21013. https://doi.org/10.1038/srep21013.
53. Alander, J.T.; Kaartinen, I.; Laakso, A.; et al. A review of indocyanine green fluorescent imaging in surgery. *Int. J. Biomed. Imaging* **2012**, *2012*, 940585. https://doi.org/10.1155/2012/940585.
54. Liu, C.; Liao, J.; Chen, L.; et al. The integrated high-resolution reflection-mode photoacoustic and fluorescence confocal microscopy. *Photoacoustics* **2019**, *14*, 12–18. https://doi.org/10.1016/j.pacs.2019.02.001.
55. Wang, Y.; Maslov, K.; Kim, C.; et al. Integrated Photoacoustic and Fluorescence Confocal Microscopy. *IEEE Trans. Biomed. Eng.* **2010**, *57*, 2576–2578. https://doi.org/10.1109/tbme.2010.2059026.
56. Cavigli, L.; Khlebtsov, B.N.; Centi, S.; et al. Photostability of Contrast Agents for Photoacoustics: The Case of Gold Nanorods. *Nanomaterials* **2021**, *11*, 116. https://doi.org/10.3390/nano11010116.
57. Kim, M.; Kubelick, K.P.; Vanderlaan, D.; et al. Coupling Gold Nanospheres into Nanochain Constructs for High-Contrast, Longitudinal Photoacoustic Imaging. *Nano Lett.* **2024**, *24*, 7202–7210. https://doi.org/10.1021/acs.nanolett.4c00992.
58. Pu, K.; Shuhendler, A.J.; Jokerst, J.V.; et al. Semiconducting polymer nanoparticles as photoacoustic molecular imaging probes in living mice. *Nat. Nanotechnol.* **2014**, *9*, 233–239. https://doi.org/10.1038/nnano.2013.302.
59. Zhang, W.; Li, Y.; Yu, Y.; et al. Simultaneous photoacoustic microscopy, spectral-domain optical coherence tomography, and fluorescein microscopy multi-modality retinal imaging. *Photoacoustics* **2020**, *20*, 100194. https://doi.org/10.1016/j.pacs.2020.100194.
60. Zhu, X.; Huang, Z.; Li, Z.; et al. Resolution-matched reflection mode photoacoustic microscopy and optical coherence tomography dual modality system. *Photoacoustics* **2020**, *19*, 100188. https://doi.org/10.1016/j.pacs.2020.100188.
61. Toy, R.; Hayden, E.; Camann, A.; et al. Multimodal *In Vivo* Imaging Exposes the Voyage of Nanoparticles in Tumor Microcirculation. *ACS Nano* **2013**, *7*, 3118–3129. https://doi.org/10.1021/nn3053439.
62. Choi, T.Y.; Choi, T.I.; Lee, Y.R.; et al. Zebrafish as an animal model for biomedical research. *Exp. Mol. Med.* **2021**, *53*, 310–317. https://doi.org/10.1038/s12276-021-00571-5.